NANOSYSTEMS:
PHYSICS, CHEMISTRY, MATHEMATICS

Original article

Manushkin A.A., et al. *Nanosystems: Phys. Chem. Math.*, 2025, **16** (1), 5–13.
http://nanojournal.ifmo.ru
DOI 10.17586/2220-8054-2025-16-1-5-13

Phase-contrast method for determining the size of the effective focal spot of a nanofocus X-ray tube

Alexey A. Manushkin[1,a], Nikolay N. Potrakhov[2], Dmitrii K. Kostrin[2,b], Karina K. Guk[2]

[1]"Diagnostika-M" LLC, Moscow, Russia

[2]Saint Petersburg Electrotechnical University "LETI", St. Petersburg, Russia

[a]manushkinaa@mail.ru, [b]dkkostrin@mail.ru

Corresponding author: A.A. Manushkin, manushkinaa@mail.ru

PACS 07.85.-m, 52.38.Ph

ABSTRACT The work is devoted to the development of a method for testing the focal spot size of nanofocus and microfocus X-ray tubes based on phase contrast radiography of test objects. The method is based on the comparison of the interference X-ray image with the calculated values obtained by the exact numerical solution of the wave equation. The high sensitivity of the method to the size of the source is ensured by the fusion of interference fringes with contrast of different signs. The formation of X-ray phase contrast images of test objects is analyzed on the basis of the wave equation using numerical modeling of the intensity profile. An analytical expression has been obtained to estimate the size of the X-ray tube focus. The results of calculations of phase contrast profiles for a nylon fishing line and a reference nanofocus test are presented.

KEYWORDS X-rays, phase contrast, interference, non-destructive testing, test object

ACKNOWLEDGEMENTS The work was carried out with the financial support of the Ministry of Education and Science of the Russian Federation (by Agreement dated February 09, 2023, No. 075-11-2023-006, state contract identifier 000000S407523Q6V0002).

FOR CITATION Manushkin A.A., Potrakhov N.N., Kostrin D.K., Guk K.K. Phase-contrast method for determining the size of the effective focal spot of a nanofocus X-ray tube. *Nanosystems: Phys. Chem. Math.*, 2025, **16** (1), 5–13.

1. Introduction

Currently, nanofocus radiography is increasingly being used in various fields of science, technology and medicine [1, 2]. In relation to the problems of flaw detection and control of electronic products with integrated circuits, it is important to use X-ray tubes with an anode voltage above 150 kV with nanometer and micrometer focus sizes. The development of nanofocus radiography in relation to the study of high-tech nanoelectronics devices and new materials requires the development of new X-ray source testing tools.

The size of the focal spot is the most important parameter determining the amount of geometric blurring and, consequently, the image quality of the objects under control. In the countries of the European Union, the EN 12543 standard "Non-destructive testing. Characteristics of focal spots in industrial X-ray systems for use in non-destructive testing" is in force. The generalized data of numerous measurements of nanofocus spots given in [1] and the results of relevant experimental studies obtained by the authors of the present work showed that the reliability and dispersion of the obtained measurement values performed in accordance with the above standards are unsatisfactory.

The standard methods for measuring the size of the effective focal spot of nanometer-sized X-ray tubes are based on the absorption of X-ray radiation in test objects made of materials that strongly absorb X-ray radiation. In addition to absorption, X-rays, when interacting with an object, experience refraction at its boundaries, which leads to the formation of a phase contrast [3, 4]. This refraction can be detected using highly coherent synchrotron X-ray sources [5, 6] or nanofocus X-ray tubes [7, 8] in the form of interference patterns at some distance from objects. The magnitude of the phase contrast critically depends on the size of the X-ray tube focus [9–12].

Numerous studies in the field of phase contrast have established a strong dependence of phase contrast on the size of the X-ray focal spot. However, as far as we know, no systematic studies have been conducted on the use of phase contrast imaging to determine the focal spot, while advanced methods of absorption contrast have been developed in a wide range of focal spot sizes up to the nanofocus region.

The formation of a two-dimensional absorption X-ray image $f(x, y)$ from an ideal point source is described within the framework of projection ray geometric optics, and the effect of size and shape on the final recorded image $g(x, y)$

is described as a convolution of the ray projection of an object with a two-dimensional distribution $h(x, y)$ of X-ray brightness along the focal spot:

$$g(x, y) = f(x, y) * h(x, y), \tag{1}$$

where the $*$ sign indicates a convolution operation.

With a high signal-to-noise ratio, reliable information not only about the size of the focus, but also its shape makes it possible to improve spatial resolution by deconvolution of the image. For example, in [13], the possibility of improving the image of bone tissues was demonstrated by taking into account the intensity distribution on the double focal spot due to the extended spiral structure of the tungsten anode.

For two-dimensional deconvolution, the two-dimensional Fourier transform can be used, as a result of which the original object can be formally restored in the domain of spatial frequencies:

$$F(u, v) = \frac{G(u, v)}{H(u, v)}, \tag{2}$$

where F, G, H are the Fourier transforms of the functions f, g, h.

In practice, in the presence of noise, it is necessary to make a more complex search for the optimal solution using a priori data on the desired distribution of $f(x, y)$ and on the nature of noise based on a reasonable balance between image sharpness and noise level.

It is shown in [14] that the two-dimensional deconvolution problem is reduced to one-dimensional deconvolution of radial profiles $I(x, y)$ of circular aperture images, resulting in a synogram of the Radon transformation of the focal spot with subsequent tomographic reconstruction. This procedure was applied to distribution of a focal spot with a diameter of 0.3 mm of a mammography tube.

In another work [15], the circular aperture method was scaled to focal spots with micron and submicron sizes. When working with nanofocus sources, test objects closely approach the focal spot at a distance of no more than a millimeter, and this makes it possible to provide a 1000× magnification when the detector is removed at a distance of about 1 m.

The low power of the nanofocus tubes, the large distance to the detector and the weak absorption contrast of the test objects cause a high level of image noise and a long signal accumulation time. For example, in [16] radiographic images of the JIMA test were obtained, with a test strip period of 150 nm. The images were obtained on a nano-CT laboratory setup at source voltages of 60 and 40 keV. The accumulation time was 10 and 20 min, respectively.

The purpose of this work is to explore the possibilities of a phase-contrast method for testing nanofocus tubes within the framework of classical principles of wave optics in order to provide practical recommendations for the development of test objects, methods of their use and the development of related software.

2. Materials and methods

To numerically calculate the phase-contrast image of a model object, Fourier optics methods based on the decomposition of the wave field into planar components were used [17]. Let's consider the wave equation for the amplitude $A(r, t)$ of a monochromatic wave propagating freely in space:

$$\Delta A - \frac{1}{v^2}\frac{\partial^2 A}{\partial t^2} = 0, \tag{3}$$

where Δ is the Laplace operator, $A(\mathbf{r}, t)$ is a function of spatial coordinates and time describing the wave field, v is the propagation velocity of the wave field. For a stationary field of monochromatic radiation

$$A(\mathbf{r}, t) = A(\mathbf{r})e^{i\omega t} \tag{4}$$

and the wave equation is simplified to a linear homogeneous Helmholtz equation:

$$\Delta A + k^2 A = 0, \tag{5}$$

where $k = \omega/v$. In vacuum, $v = c$ and $k = 2\pi/\lambda$, where λ is the wavelength of the propagating radiation. Plane waves of the form

$$A_{\mathbf{k}}(\mathbf{r}) = e^{i(\mathbf{k}\cdot\mathbf{r})}, \tag{6}$$

where $\mathbf{k}$ is the wave vector, are exact solutions of the wave equation and form the basis of functions from which the desired solution of the Helmholtz equation can be constructed:

$$A(\mathbf{r}) = \int a(\mathbf{k})e^{i(\mathbf{k}\cdot\mathbf{r})}dS_{\mathbf{k}}, \tag{7}$$

where $dS_{\mathbf{k}}$ is an element of the surface area of a sphere of radius $\mathbf{k}$, in which the wave vectors of plane waves are concentrated. Provided that $|\mathbf{k}| = k$, each possible direction $\mathbf{k} = (k_x, k_y, k_z)$ of propagation of a plane wave is given by its projections k_x and k_y onto the xy plane. Let's put $z = 0$ in formula (7), then this formula will be rewritten in the following form:

$$A(x, y, z = 0) = \int a(k_x, k_y)e^{i(k_x x + k_y y)}dk_x dk_y. \tag{8}$$

Thus, the wave field in free space is represented as a sum of plane-wave components, with expansion coefficients $a(k_x, k_y)$ determined by the Fourier expansion of the field in the plane. When a plane wave falls on an object, the phase shift of the wavefront and the curvature of the wave front are observed, and the appearance of plane-wave components of the scattered wave propagating paraxially at different angles of coherent scattering occurs.

When radiation propagates from the $z = 0$ plane to the z plane of image detection, each plane-wave component receives an additional phase multiplier $\exp(ik_z z)$, where

$$k_z = \sqrt{k^2 - k_x^2} \approx k\left(1 - \frac{k_x^2}{2k^2}\right) \approx k\left(1 - \frac{\alpha^2}{2}\right). \tag{9}$$

The interference of the incident wave and the wave scattered at an angle α forms interference fringes of size dx:

$$dx = \frac{\lambda}{2\sin\alpha}. \tag{10}$$

The angular spectrum of a coherently scattered plane wave is dominated by plane-wave components with small scattering angles. Components with large scattering angles and having smaller amplitude are formed at the edges of the object, where the phase shift in the object becomes small. Accordingly, at the final resolution of the detector, in order to observe a strong phase contrast with wider interference fringes, the detector should be removed from the object if the geometric blurriness is small. As the detector approaches the object, narrower interference fringes with less contrast are formed. The geometry of shooting a test object using the phase-contrast method is shown in Fig. 1.

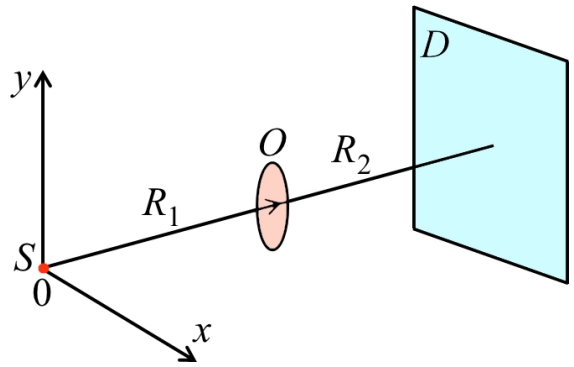

FIG. 1. Geometry of the phase-contrast shooting of the test object: S is a nanofocus source, O is a test object, D is a two-dimensional detector

In the coordinate representation, the paraxial propagation of a wave in free space from an object with a coordinate $z = 0$ to a detector with $z = R$ is expressed as a convolution of the amplitude of the initial $A(x', z = 0)$ with a Fresnel propagator:

$$A\,(x, z = R) = \int A\,(x', z = 0) \exp\left(-\frac{i\,(x - x')^2}{2R}\right) dx'. \tag{11}$$

The dx' integration regions can be divided into Fresnel zones with m indices. In the case of an incident plane wave, the radii d_m of the first Fresnel zones with small indices for the distance R from the object to the observation point are expressed by the well-known formula:

$$d_m \approx \sqrt{\lambda R m}, \quad m = 1,\, 2,\, 3\ldots \tag{12}$$

For a spherical wave on an object with distances of R_1 and R_2, the same formula with an effective diffraction distance R (lens formula) is valid:

$$\frac{1}{R_1} + \frac{1}{R_2} = \frac{1}{R}. \tag{13}$$

Thus, in the paraxial approximation, the calculation of the diffraction of an object on a spherical wave from a point source with geometric parameters R_1 and R_2 is equivalent to the calculation of the diffraction of an object on a plane wave [18]. Bringing the contrast calculation from a point source to a plane-wave case simplifies and significantly speeds up calculations and makes it possible to implement them on mobile platforms.

For $R_2 \to \infty$ the increase in R reaches the maximum value of R_1. Accordingly, the size of the first Fresnel zone and the magnitude of the phase contrast reach the limit values, which depend mainly on the difference in phase shift at the edges of this zone.

Let's determine the maximum size of the focal spot, which for a cylinder gives about 50 % of the maximum contrast from a point source. If R_1 and R_2 are the distances from the source to the object and from the object to the detector (see Fig. 1), then the factor of increasing the size of the source $f = 1 + R_2/R_1$ gives us a geometric blurriness $S = r(1 + R_2/R_1)$.

The possibility of geometrically increasing interference fringes without loss of contrast makes it possible to use amplifying screens and electronic recording devices instead of X-ray films. In order to observe a strong phase contrast, it is necessary that the width of the interference fringe $dx = \lambda/\sin\alpha$ be commensurate with the geometric blurriness. The condition of the opposite phases of the direct and scattered waves is expressed by the formula:

$$k\alpha^2 R = \pi. \tag{14}$$

From equations (11) and (14), taking into account $R \cong R_1$ at $R_2/R_1 \gg 1$, the maximum diameter d of the focal spot of the source is obtained, at which the contrast is close to half the contrast from the point source:

$$d \approx \sqrt{2}\, dx = \sqrt{\lambda R_1}. \tag{15}$$

3. Results and discussion

The numerical calculation of the phase contrast image from a point source according to the formula (11) in rectangular coordinates presents certain difficulties due to the need to represent the high-frequency modulation of a spherical wave field at a large aperture. The program used in this work to calculate the one-dimensional profile of images of model objects based on the fast Fourier transform used large amounts of RAM, and the calculation on a desktop computer with an NVIDIA GeForce RTX 2080 GPU lasted about a minute.

Figure 2 shows the intensity profiles for an ideal point source and a source with a finite size, which demonstrate the condition of strong contrast according to the formula (15).

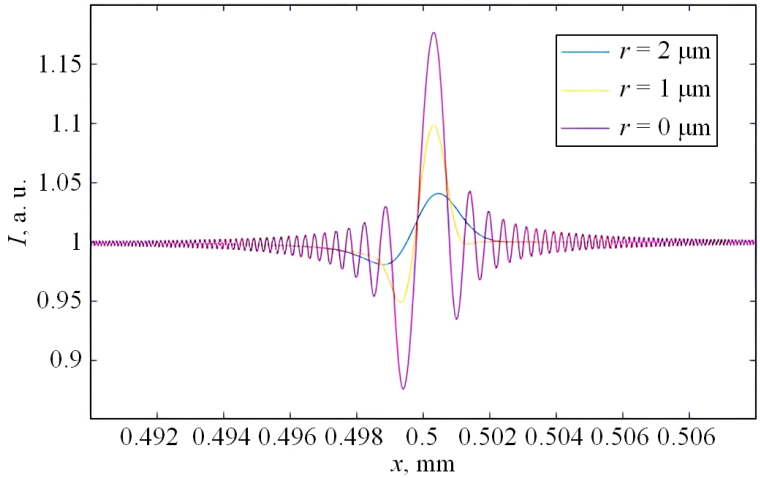

FIG. 2. Calculated intensity profiles of the phase-contrast image of the edge of a nylon fishing line with a diameter of 1 mm at a radiation energy of 60 keV for a point source and for focal spots of 1 and 2 micrometers in size ($R_1 = 50$ mm, $R_2 = 500$ mm)

Formula (15) corresponds to a focal spot diameter of 1 μm, at which the phase contrast value reaches 50 % of the contrast for a source with a zero focal spot size. When using X-ray optical transducers with a limited dynamic range or films with a nonlinear response, it is difficult to quantify the amount of contrast. The size of the focus is easier to estimate by measuring the width of the main interference maximum, which for the focal length $d = 2$ μm will double (Fig. 2). Model calculations for aluminum wire, with a refractive index about 2.7 times higher than that of nylon, show the possibility of increasing the phase contrast by 2 times and, accordingly, the possibility of increasing the signal-to-noise ratio by 4 times.

If it is necessary to check the estimated value r of the focal spot of the X-ray source, then for this purpose the minimum distance R_1 from the source to the test object should be selected according to formula (15). For example, for a spot diameter of 1 μm and energy of 60 keV, it is necessary to select a distance R_1 of the order of 50 mm. The distance R_2 is selected based on the choice of geometric magnification for a given detector resolution.

Let's consider the formation of nanofocus images on phase-modulating diffraction gratings, which are a set of periodic structures of several tungsten strips with different widths from 400 nm and thicknesses up to 10 μm, sufficient for deep phase modulation of X-ray radiation. These gratings are similar to the JIMA RT RU-02B tests designed to determine the size of the focus of X-ray tubes. The test manufacturer describes the strips as X-ray absorbing tungsten strips with a thickness of 1 μm. The calculated absorption attenuation per 1 μm of tungsten for energies from 60 to 30 keV is from 1 to 4 %. Tests of a similar design were used to obtain the resolution of scintillators [19].

It is convenient to analyze the formation of diffraction grating images in a pulsed representation based on equation (13) and formula (12), in which dx denotes the half-period of the diffraction grating. From formula (15), it is possible

to obtain the nearest effective distance R at which Fourier images of a diffraction grating with maximum contrast from a plane incident wave are formed (Talbot effect) [17]:

$$R = \frac{dx^2}{2\lambda} n, \quad n = 1,\ 2,\ 3\ldots \tag{16}$$

In the geometry of a point source, the Fourier images will be magnified by $(1 + R_2/R_1)$ times and will be observed at distances determined by the ratio [17]:

$$\frac{1}{R_1} + \frac{1}{R_2} = \frac{2\lambda}{dx^2 n}. \tag{17}$$

The Fourier images are obtained at consistently increasing intervals up to the maximum positive value of n, after which the value $(dx^2 n)/(2\lambda)$ will be greater than R_1. For $\lambda = 0.021$ nm ($E = 60$ keV) and $dx = 1$ μm, it turns out $dx^2/(2\lambda) = 23.8$ mm. This value determines the maximum distance R_1 at which condition (17) is satisfied.

Figures 3 and 4 show the calculated profiles of phase grating images for conditions of strong (far-focus mode) and weak (near-focus mode) contrast at a phase modulation depth on the diffraction grating $\pi/2$ and a focus diameter of 1 μm.

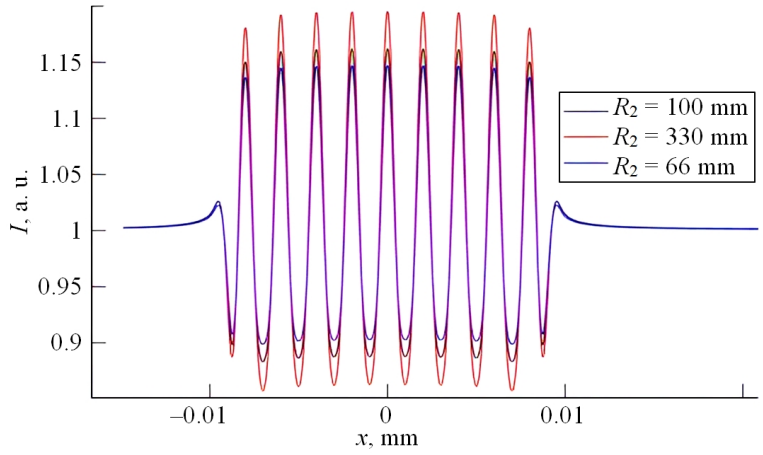

FIG. 3. Calculated contrast profiles of the test with a phase-modulating grating period of 1 μm for a radiation energy of 60 keV under shooting conditions with strong contrast ($R_1 = 33$ mm). The focus size is 1 μm

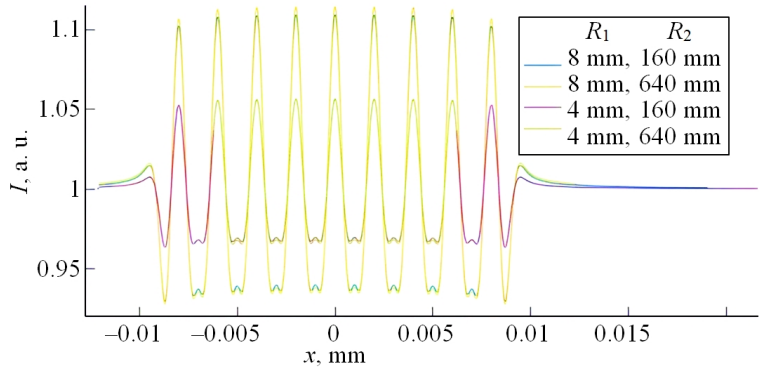

FIG. 4. Calculated contrast profiles of the test with a grating period of 1 μm for a radiation energy of 60 keV in the near-focus shooting mode. The focus size is 1 μm. The graphs are scaled along the x axis without taking into account geometric magnification

With a limited resolution of a digital matrix detector with a pixel size of more than 100 μm, it becomes necessary to bring the test closer to the focus of the source. At the same time, as shown in Fig. 4, the phase contrast determined by the difference between the maximum and minimum intensity values decreases, but remains even greater than the calculated absorption value of 4 %. Fig. 5 shows profiles for several focal spot sizes, with similar parameters $R_1 = 8$ mm, $R_2 = 640$ mm and $dx = 1$ μm.

From the above, it can be concluded that the contrast of the test image depends on the size of the focus and on the degree of transformation of the phase modulation of the grid into an amplitude one, determined by the geometry of the shooting. When the R_1 parameter is properly selected in the mode of limiting the conversion of phase modulation to amplitude, the contrast mainly depends on the size of the focus.

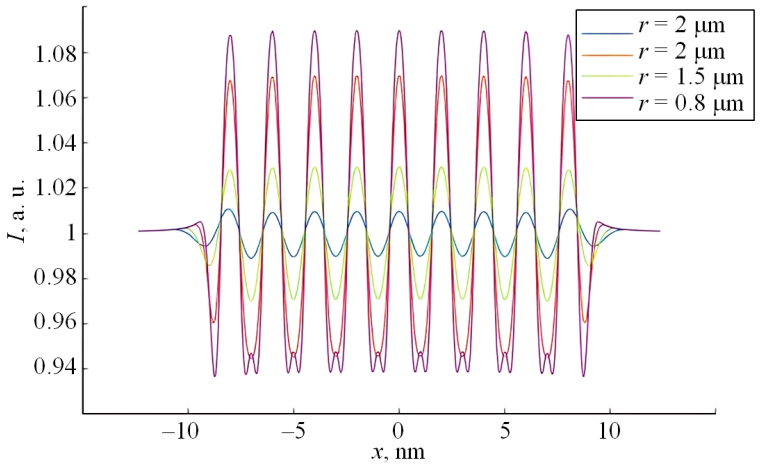

FIG. 5. Calculated diffraction grating images for different focal spot sizes. Radiation energy $E = 60$ keV, modulation depth of the lattice phase is $\pi/2$

Let's now consider the formation of a phase contrast in the braking radiation (bremsstrahlung) of an X-ray tube. The depth of phase modulation $\delta\varphi$ in the X-ray diffraction grating is determined by the phase shift, which is determined by the decrement of the refractive index δn and the thickness of the modulating layer t:

$$\delta\varphi = \frac{2\pi\delta n t}{\lambda}. \tag{18}$$

In the X-ray region of the electromagnetic spectrum, the decrement of the refractive index of a single-element substance is determined by the cross section of elastic X-ray scattering on an atom and the density of the substance:

$$\delta n = \frac{N r_e}{2\pi}\lambda^2, \tag{19}$$

where N is the electron density, r_e is the classical electron radius.

For tungsten, the refractive index decrement is $8.59 \cdot 10^{-7}$ for 60 keV. Thus, in order to obtain a phase shift of $\pi/2$, 6 micrometers of tungsten layer are needed.

To obtain deep phase modulation with a spatial frequency of 1 μm, high-tech methods for the formation of high-aspect microstructures based on liquid or plasma-chemical etching of silicon, currently used to create X-ray optical elements of Talbot–Laue interferometers, can be used [20].

The phase contrast distribution differs significantly for different values of the Fresnel number $NF = a^2/(\lambda R)$, where a is the size of the structure in the depicted object, $R \approx R_1$ (at $R_2 \gg R_1$) is the effective diffraction distance. The regions of the far (Fraunhofer diffraction region) and near fields (field of geometric optics) and the intermediate region (Fresnel diffraction region) are determined by the corresponding NF values: $NF \ll 1$, $NF > 1$, $NF \approx 1$. Diffraction effects occur not only with phase modulation of the wavefront, but also with amplitude modulation of radiation by X-ray absorbing objects.

The width of the diffraction blur on the detector at magnification M is determined by the expression:

$$\sigma = M\sqrt{\lambda R} \approx M\sqrt{\lambda R_1}. \tag{20}$$

To reduce the diffraction blurring of the image of the test object edges smaller than the size of the nanofocus spot, it is necessary to bring the object close to the source. For example, for an energy of 60 keV ($\lambda = 0.021$ nm) and a distance R_1, according to formula (20), this distance should be less than 0.5 mm.

The results of numerical calculation of diffraction blurring of an X-ray absorbing test periodic structure with a period of 100 nm are shown in Fig. 6. The normalized amplitude $A(x)$ of the test object was calculated using the formula $A(x) = 1 - cf(x)$, where $c = 0.02$ is the absorption amplitude decrease expressed as a percentage, and $f(x)$ is the normalized amplitude modulation profile after an X-ray mask with a strip width of 100 nm. The calculation results show a diffraction reduction in the contrast of the nanoobject.

In support of the conclusion about diffraction blurring of strip images, Fig. 7 shows radiographic absorption images of the JIMA test, with a period of 150 nm test strips, adapted from [16]. It is noteworthy that with a greater contrast of the wide boundaries of the test, the distinguishability of 150 nm strips for 40 kVp is worse than for 60 kVp, despite the lower noise level.

In our opinion, the authors of this work, performed at a high experimental level, mistakenly explained this difference by a different choice of the digital range of image representation. In fact, with the high accuracy of nanoscopy and the lower rigidity of X-ray radiation, the diffraction envelope of nanoscale obstacles by X-ray radiation manifested itself, which reduced the modulation amplitude.

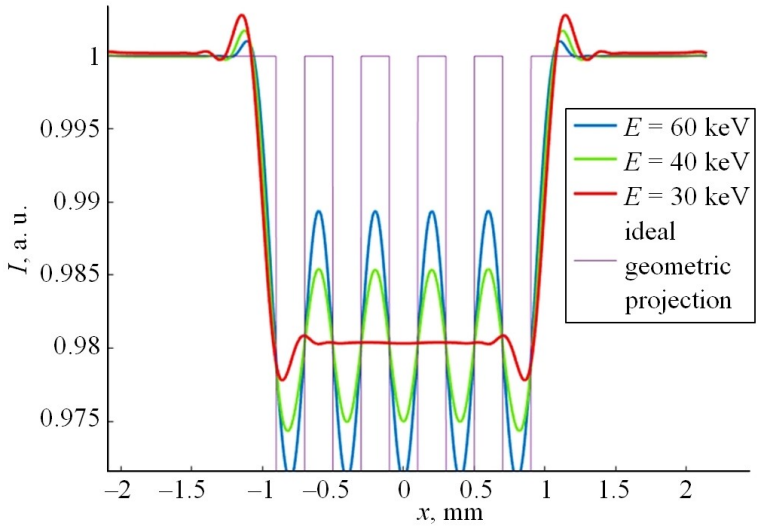

FIG. 6. Calculated profile of the normalized intensity modulation on the detector for different energies. $R_1 = 0.5$ mm, $R_2 = 1000$ mm, the focal spot size is 100 nm

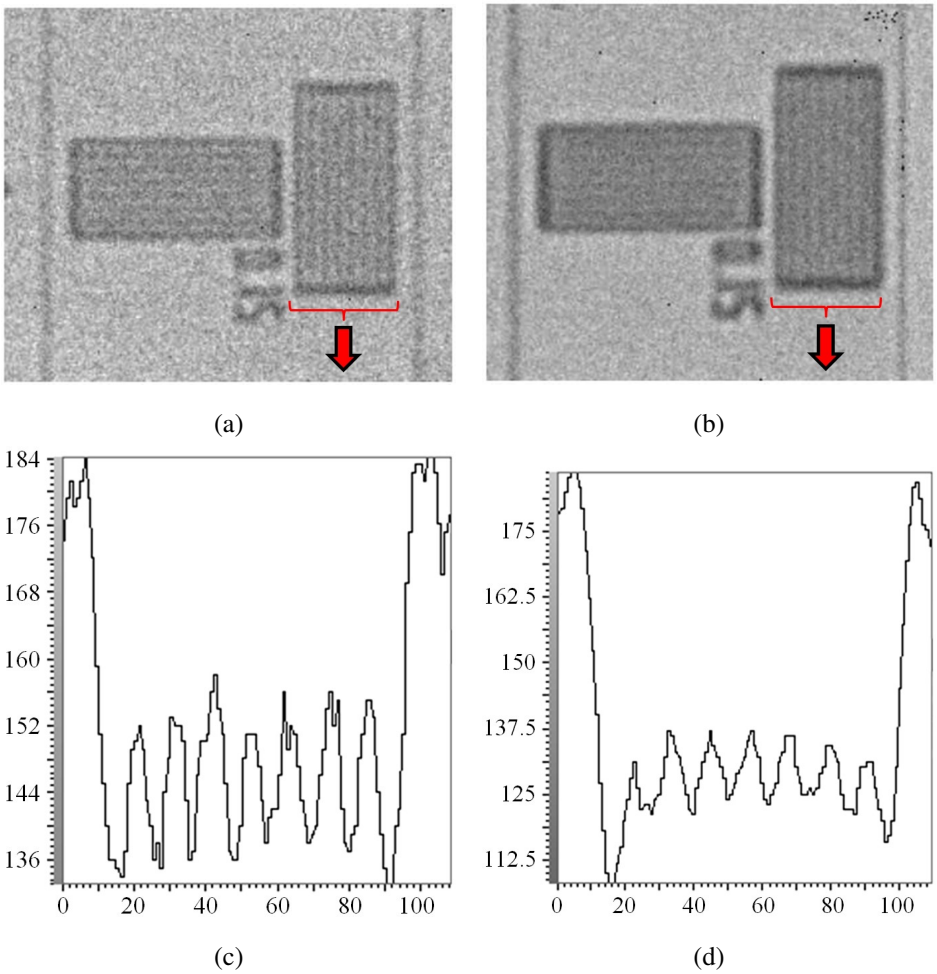

FIG. 7. Images of the test object (a), (b) and cross-section profiles of vertical test images after processing with a median filter of size 1×201 (c), (d): (a), (c) – 60 kVp, 1.15 μA, 10 min; (b), (d) – 40 kVp, 0.7 μA, 20 min

Let's turn now to the use of cylindrical test objects. Since the phase incursion at the line boundary will be small at nanofocus distances, and the resulting phase contrast is very weak, it is advisable to use high-density materials such as mercury or gold (Fig. 8).

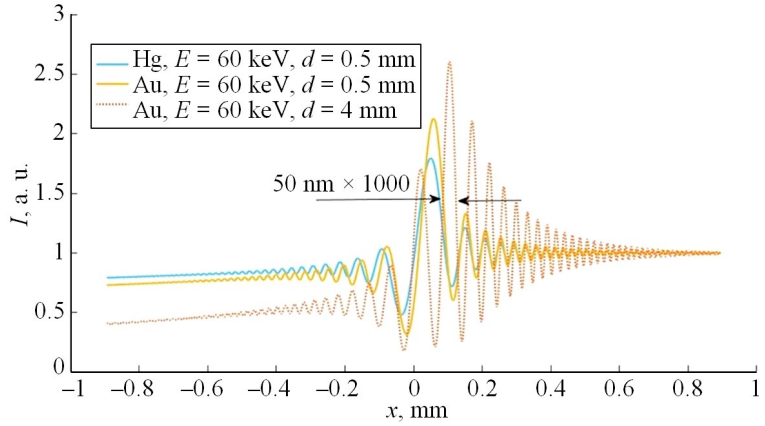

FIG. 8. Results of the model calculation of the phase profile at the boundaries of test cylindrical objects from a point source at $R_1 = 0.5$ mm, $R_2 = 500$ mm

As can be seen from the above result, the use of test objects of high-density materials with a high refraction index makes it possible to obtain from a point source a phase-contrast picture of edge diffraction with a spatial resolution of up to 50 μm with a magnification factor of $\times 1000$. The high level of phase contrast opens up potential possibilities for monitoring the size and position of the focal spot in real time and its corresponding correction during data collection.

4. Conclusion

The considered phase-contrast method for determining the focal spot of nanofocus and microfocus X-ray tubes using simple macroscopic test objects and reference phase-modulating periodic microstructures is characterized by high sensitivity to the parameters of nanofocus tubes in the size range from hundreds of nanometers to several micrometers. To determine the optimal shooting geometry and the correct interpretation of images of test objects, it is advisable to use the accompanying software.

It can also be noted that not only the focal spot itself can be adjusted by affecting the focusing system, but also the image itself can be corrected. In the continuation of the ongoing research, it is planned to conduct experiments on a wide range of real X-ray tubes for a more detailed comparison of experimental data and simulation results.

References

[1] Staroverov N.E. A method for automated control of electronic components on microfocus X-ray images. *J. of the Russian Universities. Radioelectronics*, 2021, **24** (4), P. 27–36.
[2] Potrakhov N.N., Gryaznov A.Yu., Zhamova K.K., Bessonov V.B., Obodovsky A.V., Staroverov N.E., Kholopova E.D. Microfocus radiography in medicine: physical and technical features and modern means of X-ray diagnostics. *Biotechnosphere*, 2015, **5** (41), P. 55–63.
[3] Lider V.V. X-ray methods of axial phase contrast and axial holography. *Industrial Laboratory. Diagnostics of Materials*, 2015, **81** (12), P. 32–40.
[4] Nugent K.A., Paganin D., Gureyev T.E. A phase odyssey. *Physics Today*, 2001, **54** (8), P. 27–32.
[5] Snigirev A., Snigireva I., Kohn V., Kuznetsov S., Schelokov I. On the possibilities of X-ray phase contrast microimaging by coherent high-energy synchrotron radiation. *Review of Scientific Instruments*, 1995, **66** (12), P. 5486–5492.
[6] Cloetens P., Barrett R., Baruchel J., Guigay J.P., Schlenker M. Phase objects in synchrotron radiation hard X-ray imaging. *J. of Physics D: Applied Physics*, 1996, **29** (1), P. 133–146.
[7] Davis T.J., Gao D., Gureyev T.E., Stevenson A.W., Wilkins S.W. Phase-contrast imaging of weakly absorbing materials using hard X-rays. *Nature*, 1995, **373**, P. 595–598.
[8] Gryaznov A.Yu. On the possibility of obtaining phase-contrast images on microfocus X-ray sources. *Biotechnosphere*, 2010, **1** (7), P. 30–32.
[9] Shovkun V.Ya., Kumakhov M.A. Phase contrast imaging with micro focus X-ray tube. *Proceedings of SPIE*, 2006, **5943**, 594315.
[10] Shovkun V.Ya. Development of a phase-contrast mammograph in the "in-line holography" scheme. *Medical physics*, 2007, **2** (34), P. 25–34.
[11] Hertz H.M., Bertilson M., Chubarova E., Ewald J., Gleber S.-C., Hemberg O., Henriksson M., Hofsten O., Holmberg A., Lindblom M., Mudry E., Otendal M., Reinspach J., Schlie M., Skoglund P., Takman P., Thieme J., Sedlmair J., Tjornhammar R., Tuohimaa T., Vita M., Vogt U. Laboratory X-ray micro imaging: Sources, optics, systems and applications. *J. of Physics: Conference Series*, 2009, **186** (1), 012027.
[12] Bavendiek K., Ewert U., Riedo A., Heike U., Zscherpel U. New measurement methods of focal spot size and shape of X-ray tubes in digital radiological applications in comparison to current standards. *Proceedings of the "18th World Conference on Nondestructive Testing"*, Durban, South Africa, 2012, **346**.
[13] Dougherty G., Kawaf Z. The point spread function revisited: image restoration using 2-D deconvolution. *Radiography*, 2001, **7** (4), P. 255–262.
[14] Di Domenico G., Cardarelli P., Contillo A., Talbi A., Gambaccini M. X-ray focal spot reconstruction by circular penumbra analysis – Application to digital radiography systems. *Medical Physics*, 2016, **43** (1), P. 294–302.
[15] Bicher B.A., Meli F., Kung A., Sofiienko A. Traceable x-ray focal spot reconstruction by circular edge analysis: from sum-microfocus to mesofocus. *Measurement Science and Technology*, 2022, **33** (7), 074005.

[16] Nachtrab F., Firsching M., Uhlmann N., Speier C., Takman P., Tuohimaa T., Heinzl C., Kastner J., Larsson D.H., Holmberg A., Berti G., Krumm M., Sauerwein C. NanoXCT: development of a laboratory nano-CT system. *Proceedings of SPIE*, 2014, **9212**, 92120L.
[17] Goodman J.W. *Introduction to Fourier optics*. Roberts and Company Publishers, Greenwood Village, 2005, 491 p.
[18] Cowley J.M. *Diffraction physics*. North Holland Publishing, Amsterdam, 1995, 488 p.
[19] Shao W., He T., Wang L., Wang J.X., Zhou Y., Shao B., Ugur E., Wu W., Zhang Z., Liang H., de Wolf S., Bakr O.M., Mohammed O.F. Capillary manganese halide needle-like array scintillator with isolated light crosstalk for micro-X-ray imaging. *Advanced Materials*, 2024, **36** (21), e2312053.
[20] Pfeiffer F., Bech M., Bunk O., Donath T., Henrich B., Kraft P., David C. X-ray dark-field and phase-contrast imaging using a grating interferometer. *J. of Applied Physics*, 2009, **105** (10), 102006.

Submitted 2 October 2024; revised 20 November 2024; accepted 28 November 2024

Information about the authors:

Alexey A. Manushkin – "Diagnostika-M" LLC, Volgogradskiy, 42, Moscow, 109316, Russia; ORCID 0009-0009-8428-9588; manushkinaa@mail.ru

Nikolay N. Potrakhov – Saint Petersburg Electrotechnical University "LETI", Professora Popova, 5, St. Petersburg, 197022, Russia; ORCID 0000-0001-8806-0603; nnpotrahov@etu.ru

Dmitrii K. Kostrin – Saint Petersburg Electrotechnical University "LETI", Professora Popova, 5, St. Petersburg, 197022, Russia; ORCID 0000-0002-6284-0246; dkkostrin@mail.ru

Karina K. Guk – Saint Petersburg Electrotechnical University "LETI", Professora Popova, 5, St. Petersburg, 197022, Russia; ORCID 0000-0002-4968-7857; kkguk@etu.ru

Conflict of interest: the authors declare no conflict of interest.